Journal of Materials Chemistry C

PAPER

Check for updates

A probe of the radiation field magnetic component based on octahedral Yb^{3+} in the CaNbGa garnet – CNGG – single crystal†

Jorge Omar Álvarez-Pérez, [ID] José María Cano-Torres, [ID] María Dolores Serrano, [ID] Concepción Cascales [ID] and Carlos Zaldo [ID] *

In a disordered Yb^{3+}-doped CaNbGa garnet – CNGG – single crystal, it is shown that octahedral Yb centers exist up to a solubility limit of about 5×10^{18} cm^{-3} in addition to the well known dodecahedral Yb which incorporates to a much larger density $\sim 10^{21}$ cm^{-3}. Despite the low density of the octahedral Yb, the presence of a symmetry center for this garnet site forbids electric dipole (ED) transitions, thus magnetic dipole (MD) spectroscopic contributions are observed with an intensity similar to that of ED ones. Because of the easy growth of this garnet, the potential application of these two contributions for probing the magnetic field component radiated by plasmonic structures is discussed on the basis of time-resolved spectroscopy, since ED Yb^{3+} photoluminescence is about one order of magnitude faster than MD $^2F_{5/2} \rightarrow {}^2F_{7/2}$ ($\Delta J = +1$) emissions for the 0.3 at%Yb:CNGG crystal. Channels appropriated for room temperature operation can be excited at $\lambda_{EXC} = 960.3$ nm, while sensed at $\lambda_{EMI} = 1022$ nm for the short-lived ED reference channel and $\lambda_{EMI} = 998$, 1011, 1068 or 1080 nm for the long-lived MD signal channel.

1. Introduction

Energy levels of trivalent lanthanides (Ln^{3+}) are characterized by $^{2S+1}L_J$ multiplets further split by the crystal field (CF) of a host in m$_J$ levels. Intraconfigurational electronic transitions between these multiplets are most often induced by light–matter interactions mediated by electric fields through forced electric dipole (ED) transitions, but also include magnetic dipole (MD) interactions, particularly notable for transitions between multiplets with $\Delta J = 0$ or ± 1.[1] Although it is usually assumed that MD transitions are $\sim 10^5$ times weaker than ED ones, their relative intensity in fact depends on the specific selection rules. In hosts where ED transitions are weak or even strictly forbidden, as when Ln^{3+} are incorporated at sites with a center of symmetry, the intensity of MD transitions can be dominant.

Stimulated by recent advances in optical plasmonic-based metamaterials and nanophotonics, a variety of ways to exploit MD transitions of Ln^{3+} have been proposed: theoretically, as the building blocks for homogeneous negative index materials,[2] or experimentally, as probes for the study of local magnetic fields in metamaterials, in a very simple approach that consists of placing the MD probe at the metamaterial surface, and if this resonance frequency corresponds to the spectral range of the field enhancement, spectral changes in intensity or shape may be observed in comparison with other magnetic dipoles outside the system or with some reference ED emission in the same system.[3–7] Furthermore, experimental studies by using the competition between ED and MD processes have shown the way for achieving a strong enhancement of MD emission[8] and also to broadly tune the emission spectra.[9]

For the above indicated sensing purposes, previous studies have involved mainly the visible $^5D_0 \rightarrow {}^7F_1$ MD transition of Eu^{3+}, in probing systems based on Eu-doped Y$_2$O$_3$ thin films,[7–9] dispersions of Eu-doped organic systems in polymeric thin films,[3,4,6] or Eu-doped Y$_2$O$_3$ NPs (about 60 nm).[10] The specific advantage of using Eu^{3+} is the coexistence of the nearly pure MD $^5D_0 \rightarrow {}^7F_1$ ($\lambda \approx 590$ nm) transition and the ED $^5D_0 \rightarrow {}^7F_2$ ($\lambda \approx 615$ nm) transition used as the reference. Other Ln^{3+} emissions which have been tested with the same aim are mixed MD–ED transitions in the near-infrared (NIR) range, for instance the overlapping $^4F_{9/2} \rightarrow {}^6F_{11/2} + {}^6H_{9/2}$ ($\lambda \approx 734$ nm) emissions of Dy^{3+},[11] the also overlapping $^1G_4 \rightarrow {}^3H_5$ ($\lambda \approx 784$ nm) and $^3H_4 \rightarrow {}^3H_6$ ($\lambda \approx 800$ nm) emissions of Tm^{3+},[11] or the $^4I_{13/2} \rightarrow {}^4I_{15/2}$ ($\lambda \approx 1.5$ μm) transition of Er^{3+},[12] in all cases by using the corresponding doped Y$_2$O$_3$ thin films.

Instituto de Ciencia de Materiales de Madrid, Consejo Superior de Investigaciones Científicas, c/Sor Juana Inés de la Cruz 3, 28049 Madrid, Spain.
E-mail: cezaldo@icmm.csic.es

† Electronic supplementary information (ESI) available: (i) Detailed comparative optical spectroscopy of dodecahedral and octahedral Yb^{3+} centers in CNGG crystals. (ii) Detailed procedures of crystal field analyses applied to octahedral Yb^{3+} centers in 0.3 at%Yb:CNGG crystals. (iii) Crystal field splitting of ^2F_J Yb^{3+} levels and the barycenter law. See DOI: 10.1039/d0tc01608j

7882 | *J. Mater. Chem. C*, 2020, **8**, 7882–7889

This journal is © The Royal Society of Chemistry 2020

The near-infrared (NIR) range from 800 to 1100 nm has several advantages over other spectral regions. As compared to the visible (characteristic of Eu^{3+}), micron-sized plasmonic nanostructures are much easier to fabricate than nano-sized ones and their resonances exhibit higher-quality factors due to lower ohmic losses. However, as compared with the $^4I_{13/2} \rightarrow {}^4I_{15/2}$ Er^{3+} transition at $\lambda \approx 1.5$ μm, emissions at $\lambda < 1100$ nm can be observed using standard Si photodetector technology, which simplifies the detection process. Moreover, among MD Ln^{3+} emissions at this wavelength range, those that can be pumped at the NIR will be the better candidates to be used. From the above considerations the $^2F_{5/2} \leftrightarrow {}^2F_{7/2}$ transitions of Yb^{3+} (typically $\lambda_{EXC} \approx 940–980$ nm and $\lambda_{EMI} \approx 980–1060$ nm) in a centrosymmetric crystal site are very interesting options. The simple two-state energy structure of Yb^{3+} means that MD emission can account a significant contribution to the overall decay. In fact, relatively long Yb^{3+} lifetime (τ) characteristics of MD transitions have been measured for Yb-doped BaF_2 and SrF_2 fluorites ($\tau = 9.72$ ms and 8.20 ms, respectively), as well as for Rb_2NaYF_6 elpasolite ($\tau = 10.84$ ms) crystals, with Yb^{3+} at centrosymmetric sites of cubic eightfold and perfect octahedral coordination,[13] respectively, in both cases with calculated MD branching ratios of ~50%.[12]

Cubic garnets $A_3M_2N_3O_{12}$ with space group $Ia\bar{3}d$ (No. 230) offer simultaneously non centrosymmetric dodecahedral 24c sites (A) and octahedral 16a centrosymmetric sites (M) to host Ln. An illustration of the garnet structure can be seen in the general view given in Fig. 1a. Fig. 1b shows the coordination of dodecahedral AO_8 and octahedral MO_6 garnet sites. Further drawings showing other atomic arrangements can be seen for instance in ref. 14. The Ln^{3+} distribution over 24c and 16a garnet sites is a topic which has been addressed with several purposes and under different approaches.[15–23] The main factor governing the site preference of Ln^{3+} in the garnet structure is the ionic size, in such a way that garnets with any Ln^{3+} cation occupying the dodecahedral 24c site are known,[15] and only the smallest size Ln^{3+} cations, typically Dy^{3+} to Lu^{3+} and also Y^{3+} or Sc^{3+}, are able to enter into the octahedral 16a site, even up to its complete filling, but in this case a 24c cation with a considerably large size, for example Ca^{2+} in the germanate series $Ca_3Ln_2Ge_3O_{12}$,[18] including $Ca_3Y_2Ge_3O_{12}$,[20] is required, thus the relative sizes of 24c and 16a cations also play a role. The presence of Yb^{3+} in

both garnet sites would offer the possibility of having the MD probe and ED reference ions in the same tested volume minimizing uncertainties related to excitation and detection processes, but so far the properties of Yb coexisting in both garnet sites have not been properly documented. Either the studies are limited to crystallographic aspects,[16,17,20] or the spectroscopic-based proposals[21,23] are not soundly supported by crystallographic data and/or crystal field (CF) interaction calculations.

In this work we present the first report and characterization of the $^2F_{5/2}(n') \leftrightarrow {}^2F_{7/2}(n)$ MD transitions of Yb^{3+} at the octahedral 16a (centrosymmetric C_{3i} symmetry) site of the CaNbGa garnet (thereafter CNGG). The host selection is based on the large Ca^{2+} ionic size filling the dodecahedral site, see before, while a large variety of ionic filling (Nb^{5+}, Ga^{3+} and even vacancies) is found for the octahedral and tetrahedral sites of this garnet composition. The occupancy of the 24c dodecahedral site of the CNGG garnet by Yb^{3+} is well documented from both crystallographic and spectroscopic points of view.[24–27]

The emphasis of the present work is the study of Yb^{3+} in the octahedral 16a CNGG garnet site. Through low temperature (6 K) optical absorption (OA) and photoluminescence (PL) spectra followed by the modeling of CF interactions, it has been possible to establish the sequence of 16a Yb^{3+} energy levels as a well-separated set with regards to those of Yb^{3+} at the 24c dodecahedral site. The lifetime associated with the 16a Yb^{3+} $^2F_{5/2} \rightarrow {}^2F_{7/2}$ MD emissions has been also measured, and the MD branching ratio has been calculated as $\beta_{MD} = 50\%$, a value that equals those of previously indicated for Yb^{3+} in centrosymmetric sites of fluoride-based hosts.[12] Furthermore, by using their different kinetics, ED and MD Yb^{3+} PL contributions have been separated even at room temperature (RT), opening the possibility of its application as a sensor for the magnetic field radiation in plasmonic systems.

2. Methods

2.1 Crystal growth
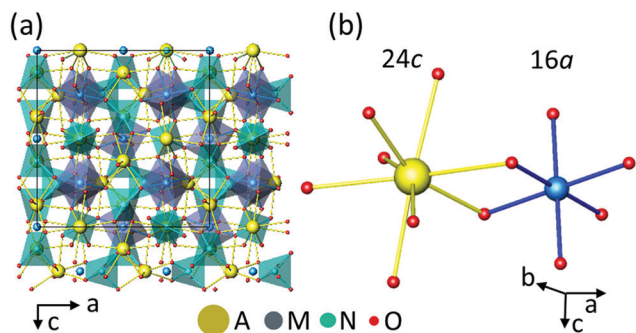
Fig. 1 (a) General view of the $A_3M_2N_3O_{12}$ garnet structure. (b) Oxygen coordinations of the AO_8 24c dodecahedra and MO_6 16a octahedra.

platinum wire was used as the seed, which was rotated and pulled simultaneously. Samples for optical purposes were obtained by crystal cutting and polishing using conventional methods.

2.2 Structural and compositional analyses

Due to the low Yb^{3+} doping (nominally 0.3 at% with regard to the dodecahedral site occupancy) of the currently studied 0.3 at%Yb:CNGG crystal, its structure should be very similar to that described for the undoped CNGG single crystal in one of our previous studies.[14] So, we shall adopt the crystal formula previously determined by the refinement of single crystal X-ray diffraction (XRD) data, i.e. $\{Ca_{0.985}\square_D\}_3[Nb_{0.625}Ga_{0.372}\square_O]_2$-$(Ga_{0.821}Nb_{0.102}\square_T)_3O_{12}$, $\square$ stating for vacancies at 24c dodecahedral (curly brackets), 16a octahedral (square brackets) and 24d tetrahedral (parentheses) sites.

The low concentration of Yb in the studied garnet prevents their compositional determination using XRD or X-ray fluorescence methods. However, these methods were successfully used for heavily (>10 at%) Yb-doped crystals. Thus, the actual Yb content of the used 0.3 at%Yb:CNGG crystal was determined by comparison of the integrated RT OA in this and in heavily Yb-doped crystals. This methodology provides a 0.08 at%Yb content for the grown crystal with regards to the dodecahedral occupancy.

2.3 Spectroscopic techniques

OA in the visible and NIR region was determined by using a Varian spectrophotometer, model Cary 5E, with a limiting spectral resolution of 0.04 nm at $\lambda \approx 1000$ nm. An extensive 6 K OA study in the whole visible region using a thick (≈ 5.1 mm) 0.3 at%Yb:CNGG sample discarded the contamination with any Ln different to the studied Yb^{3+}. PL was excited either in a continuous wave (cw) with a tunable Ti-sapphire laser or pulsed (10 Hz) with a tunable Quanta-Ray MOPO-HF system providing ns laser pulses. PL light was dispersed in a SPEX (f = 34 cm) spectrometer and detected using a 77 K cooled Ge photodiode in cw experiments, or with a Hamamatsu InP/InGaAs phototube (model H10330A-75) in lifetime measurements and time-resolved spectroscopy. In cw PL experiments the laser beam was chopped at ≈ 200 Hz and the PL signal recovered with a lock-in amplifier. Yb^{3+} lifetime measurements were carried out using a thin crystal plate (60 μm) in order to minimize emission reabsorption. Time-resolved spectroscopy was discriminated by a Stanford Research SR400 photon counter. For 6 K optical spectroscopic measurements a He close-cycle cryostat connected to a suitable temperature controller was used.

3. Results

The OA and PL spectra of Yb^{3+} in the CNGG host originate from electronic transitions between ground $^2F_{7/2}$ and excited $^2F_{5/2}$ Yb^{3+} multiplets. Both, the D_2 and C_{3i} local symmetries of the dodecahedral 24c and octahedral 16a garnet sites, respectively, split these multiplets into four $^2F_{7/2}$ (n = 0, 1, 2, 3) and three $^2F_{5/2}$ (n' = 0', 1', 2') Kramers doublets.
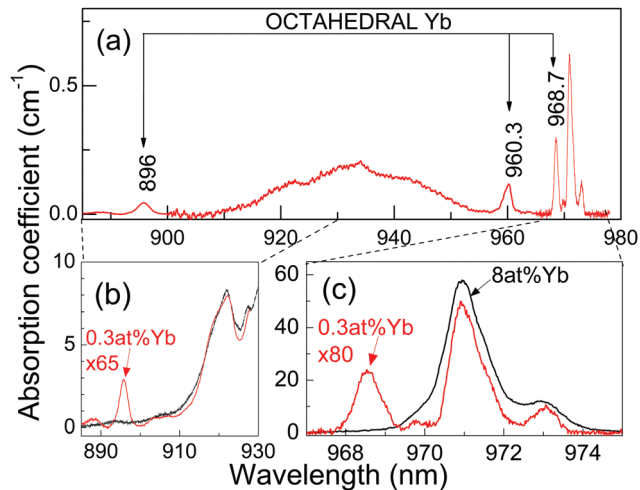

Fig. 2 (a) 6 K optical absorption spectrum of the 0.3 at%Yb:CNGG crystal (red line), and its comparison with that of the 8 at%Yb:CNGG crystal (black line) for (b) $^2F_{7/2}(0) \rightarrow {}^2F_{5/2}(2')$ and (c) $^2F_{7/2}(0) \rightarrow {}^2F_{5/2}(0')$ Yb^{3+} transitions.
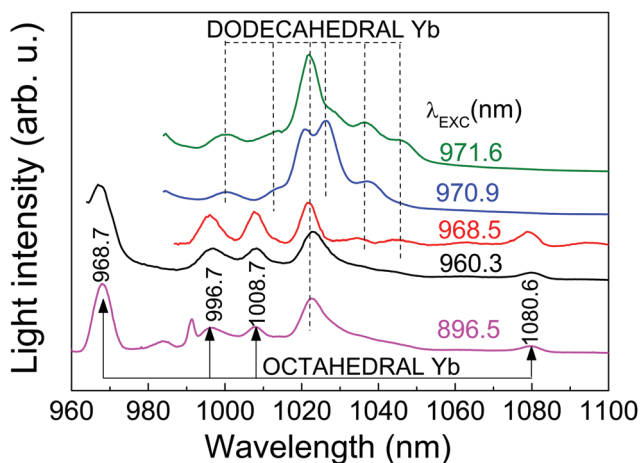

Fig. 3 Comparison of the 6 K photoluminescence spectra assigned to the octahedral 16a (λ_{EXC} = 896.5, 960.3 or 968.5 nm) and dodecahedral 24c (λ_{EXC} = 970.9 and 971.6 nm) Yb^{3+} in the 0.3 at%Yb:CNGG single crystal.

The Yb^{3+} spectra of heavily doped (>1 at%Yb) CNGG crystals have been previously studied in detail.[14,24–27] So far, the crystallographic and spectroscopic studies only provided evidence for Yb incorporation in the dodecahedral 24c site. The 6 K OA and PL spectra consist in inhomogeneously and thermally broadened bands which hamper the accurate determination of some Yb^{3+} energy levels. Fig. 2 and 3 show selected examples of the optical contributions of dodecahedral Yb in CNGG, while a more extensive dodecahedral Yb spectroscopic review is provided in the ESI.†

The only well resolved band in the 6 K spectra of 8 at%Yb: CNGG crystals is $^2F_{7/2}(0) \leftrightarrow {}^2F_{5/2}(0')$ (shortly, 0 $\leftrightarrow$ 0') at λ = 970.9 nm (see Fig. 2c). Even this band is largely broadened by the different crystalline environments coexisting around the dodecahedral 24c site of Yb^{3+}, since the spectral position of this 0 $\leftrightarrow$ 0' transition is mainly related to the electric charge of cations/vacancies occupying the two edge-sharing tetrahedra

7884 | J. Mater. Chem. C, 2020, 8, 7882–7889

This journal is © The Royal Society of Chemistry 2020

at the shortest distance ($\sim$3.12 Å) from the central 24c Yb^{3+}.[24] In fact, the small OA band at λ = 973 nm corresponds to a dodecahedral Yb^{3+} center linked to a vacant edge-sharing tetrahedron.[24]

The 6 K OA (Fig. 2) and PL (Fig. 3) spectra of the 0.3 at%Yb:CNGG crystal show bands not observable in the corresponding spectra for heavily doped >1 at%Yb:CNGG crystals. The new well-resolved OA bands peak at 968.7 nm (10 323 cm^{-1}), 960.3 nm (10 413 cm^{-1}) and 896 nm (11 161 cm^{-1}), while characteristic PL emissions at 968.7 nm, 996.7 nm, 1008.7 nm and 1080.6 nm are observed when exciting any of the three above listed OA bands (see Fig. 3). The absorption intensity of this new band set reaches 40% when the 968.7 nm new OA is compared with that of the dodecahedral Yb 0 $\leftrightarrow$ 0' transition at λ = 970.9 nm, see Fig. 2c. These new OA and PL band sets indicate the actual presence of a second type of Yb center coexisting in the garnet structure with the main dodecahedral Yb^{3+} center but with a much lower solubility limit, and thus, although present with low density, its contribution is not observable in the spectrum of the heavily doped Yb:CNGG crystals. In the following we show that this new center is compatible with the assumption of Yb^{3+} located at the octahedral 16a garnet site, and hereafter we shall refer to it as octahedral Yb.

Therefore, from the OA and PL bands experimentally determined for the octahedral Yb^{3+} center in CNGG, the complete set of Yb^{3+} energy levels can be established as 0, 290, 410 and 1069 cm^{-1} for the ground $^2F_{7/2}$ (0, 1, 2, 3), and 10 323, 10 413 and 11 161 cm^{-1} for the excited $^2F_{5/2}$ (0', 1', 2') multiplets.

In a further attempt to correlate these energy levels with the octahedral C_{3i} ($\equiv S_6$) symmetry of the 16a garnet site, a parametrization of CF effects in this site has been carried out. Since the large number of CF parameters accounting for the C_{3i} symmetry makes it unrealistic for any CF modeling to reproduce the sequence of Yb^{3+} energy levels, the often followed "descent of symmetry" procedure has considered the tetragonal bypiramidal D_{4h} symmetry as the better approach, *i.e.* the higher symmetry polyhedron with coordination number CN = 6 that can be regarded as a distortion of an octahedron O_h whose fourfold rotation axis is chosen as the main axis. For the D_{4h} symmetry the CF potential is described by B_0^2, B_0^4, B_4^4, B_0^6 and B_4^6 CF parameters, preliminary O_h, B_0^4 and B_0^6 being the only independent parameters whose values were initially obtained by using the semi-empirical Simple Overlap Model.[29] Details of the procedure for the CF parametrization of 16a Yb^{3+} energy levels in CNGG are given in the ESI.† The energy levels of 16a Yb^{3+} in CNGG were adequately reproduced by using the set of free ion and D_{4h} CF parameters included in Table 1.

The $^2F_{5/2}$ Yb^{3+} PL intensity decay kinetics has been also studied as a further signature of the different symmetry of the two (octahedral and dodecahedral) Yb^{3+} centers observed in the 0.3 at%Yb:CNGG crystal. The $^2F_{5/2}$ Yb^{3+} PL time constant (τ) after 970–973 nm excitation through the $^2F_{7/2}(0) \rightarrow {}^2F_{5/2}(0')$ Yb^{3+} transition in the dodecahedral centers was shown to vary in the τ = 800–450 μs range depending on the selected excitation/emission wavelength, *i.e.* the inhomogenously modified dodecahedral center selected.[24] The increase of the Yb concentration

Table 1 Free ion (E^0 and ζ) and D_{4h} (B_0^2, B_0^4, B_4^4, B_0^6 and B_4^6) crystal field parameters (in cm^{-1}) used to reproduce the sequence of $^2F_{7/2}$ and $^2F_{5/2}$ energy levels of 16a Yb^{3+} in the CNGG crystal

Parameter		Yb^{3+} energy levels		
		Label	Observed (cm^{-1})	Calculated (cm^{-1})
E^0	4809.4	$^2F_{7/2}(0)$	0	−3.4
ζ	2905.3	$^2F_{7/2}(1)$	290	288
B_0^2	−64	$^2F_{7/2}(2)$	410	409
B_0^4	2375	$^2F_{7/2}(3)$	1069	1076
B_4^4	1844	$^2F_{5/2}(0')$	10 323	10 328
B_0^6	−210	$^2F_{5/2}(1')$	10 413	10 416
B_4^6	251	$^2F_{5/2}(2')$	11 161	11 153

further reduces this time constant. An example of the PL kinetics is shown in Fig. 4a.

The octahedral Yb center of the 0.3 at%Yb:CNGG crystal exhibits completely different PL intensity decay kinetics, see Fig. 4b. Its time extent widely covers the 10 ms range, it is more sensitive to the sample heating from 6 K to RT than in the dodecahedral case and most often a non-single exponential behavior is observed. The PL decay kinetics excited at λ_{EXC} = 960.3 nm are basically independent of the monitored wavelength
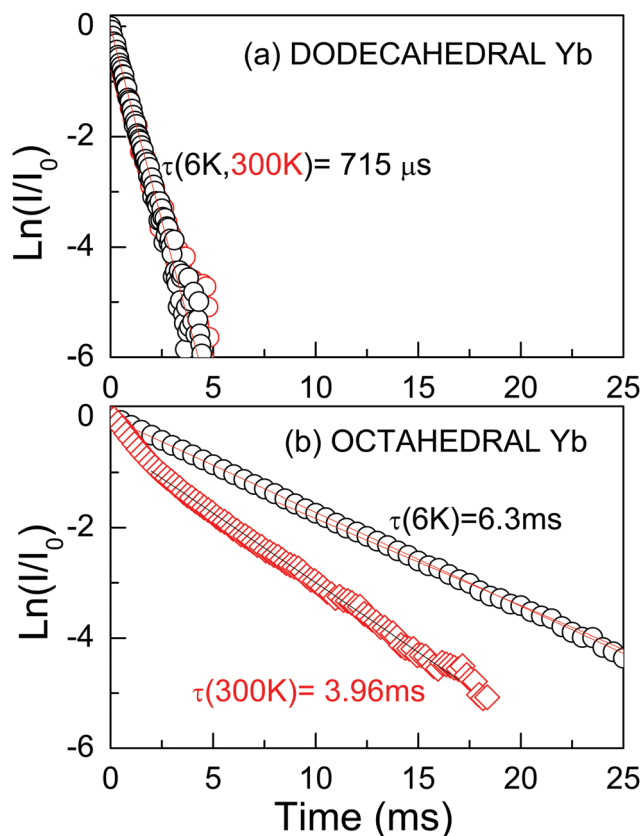

Fig. 4 Comparison of the $^2F_{5/2}$ photoluminescence intensity decay of the (a) dodecahedral 24c Yb^{3+} center, λ_{EXC} = 970.9 nm and λ_{EMI} = 1022 nm, and (b) octahedral 16a Yb^{3+} center, λ_{EXC} = 960.3 nm and λ_{EMI} = 1080.6 nm, of the 0.3 at%Yb:CNGG crystal. The points are the experimental results measured at 6 K (black points) and 300 K (red points). The lines are the fits of the long component of the corresponding decay.

(λ_{EMI} = 968.7 nm, 996.7 nm, 1008.7 nm or 1080.6 nm), see the ESI† (Fig. S4). They most typical show a fast decay for $t < 2$ ms and later a rather slow decay for the rest of the monitored time. This is understood as the overlapped contributions of the dodecahedral (short-lived) and octahedral (long-lived) Yb^{3+} centers. The long time tail of the decay can be fit to a single exponential law with a time constant $\tau \approx 6$–7 ms at 6 K and $\tau \approx 4$ ms at 300 K, *i.e.* the PL lifetime of the octahedral Yb^{3+} center is nearly one order of magnitude larger than that of the dodecahedral Yb one in the same crystal. This strong difference is consistent with the expected ED or MD Yb^{3+} PL contributions of these centers. For the non-centrosymmetric 24c D_2 dodecahedral site the contribution of ED transitions is expected to dominate the PL emission; thus the obtained $^2F_{5/2}$ Yb^{3+} lifetime is in the range observed for crystals hosting Yb^{3+} in similar non-centrosymmetric sites, like YAG, $\tau \approx 950$ μs,[30] NaLn(WO$_4$)$_2$ $\tau \approx 300$–500 μs,[31] or LnVO$_4$ $\tau \approx 250$–350 μs.[32] However, as stated in the Introduction, the presence of a center of symmetry forbids ED transitions, thus MD ones are observed with similar or even larger intensities than for the ED contributions. Such MD transitions are characterized by long PL lifetimes, thus the much larger lifetime obtained for the so-called Yb octahedral center may be regarded as the ultimate probe of the occupancy by Yb^{3+} in the centrosymmetric 16a crystal site of the CNGG host.

Once the origin of the described OA and PL features of the 0.3 at%Yb:CNGG crystal has been clarified thanks to 6 K spectroscopy, its application as a probe of plasmonic induced radiation fields requires operation at RT. Fig. 5 shows a comparison of the OA spectra corresponding to 0.3 at% and 11.6 at%Yb:CNGG crystals, the spectroscopy of the latter being purely dominated by the dodecahedral Yb^{3+} contributions. It is obvious that excitation of the octahedral Yb^{3+} center at RT through its $0 \rightarrow 0'$ transition at $\lambda = 968.7$ nm is not possible because with increasing temperature the relative intensity of this band decreases and overlaps with the $0 \rightarrow 0'$ (at $\lambda = 972.3$ nm) band tail corresponding to the dodecahedral Yb^{3+} center. However, the

Fig. 6 300 K time-resolved photoluminescence emission of the 0.3 at%Yb:CNGG crystal after excitation at $\lambda = 960.3$ nm for different delay and gate times. Gate width of 250 μs delay 5 μs after laser pulse excitation (representative of the dodecahedral Yb^{3+} contribution, black dashed line) and gate width of 8 ms delay 2.5 ms (representative of the octahedral Yb^{3+} center, red continuous line).

comparison of the spectra at both Yb doping concentrations shows that the octahedral Yb^{3+} $0 \rightarrow 1'$ transition at $\lambda = 960.3$ nm is clearly resolved from the background dodecahedral Yb contribution, the latter amounts to about 50% at this wavelength. Although the standard (integrated over time) cw PL spectra show little difference for excitation at the octahedral Yb^{3+} ($\lambda = 960.3$ nm) or in the side bands corresponding to the dodecahedral Yb^{3+} centers (see Fig. S3, ESI†), taking advantage of the different PL kinetics of both Yb^{3+} garnet centers, time-resolved spectroscopy can disclose the separate contributions of these two Yb^{3+} garnet centers.

Fig. 6 shows the RT time-resolved PL emission obtained for different delays and gate widths after the laser pulse (<5 ns of duration, tuned at $\lambda = 960.3$ nm) excitation. For short times (5 μs of delay and 250 μs of gate width) the PL is dominated by the short-lived ED contributions of the dodecahedral Yb^{3+} center. Correspondingly, the emission spectrum shows a broad peak at 1022 nm characteristic of the PL observed in highly doped Yb:CNGG,[24,26] which is also shown in Fig. 3 ($\lambda_{EXC} = 971.6$ nm). However, over a long time (2.5 ms of delay and 8 ms of gate width) the spectrum is quite different, and matches the emission of the octahedral Yb^{3+} shown in Fig. 3. Although the contribution of the $\lambda = 1022$ nm band is still present, this PL spectrum contains four well resolved emissions at $\lambda = 998$, 1011, 1068 and 1080 nm, with intensities 2.80, 2.56, 2.94 and 3.76 times those corresponding to the dodecahedral Yb^{3+} contributions at the same wavelengths, respectively. The origin of the 1068 nm RT emission is related to the thermal redistribution of the $^2F_{5/2}$ electronic population, and corresponds to the $^2F_{5/2}(1') \rightarrow {}^2F_{7/2}(3)$ transition of the octahedral Yb^{3+} center.

4. Discussion

From 6 K OA and the excitation/emission PL spectra shown in Fig. 2 and 3, it has been disclosed that along the predominant
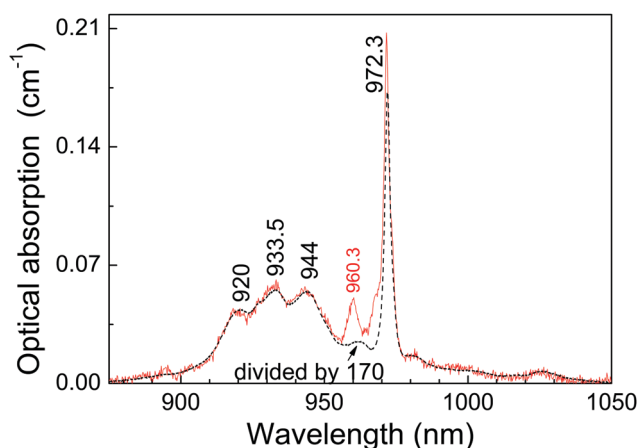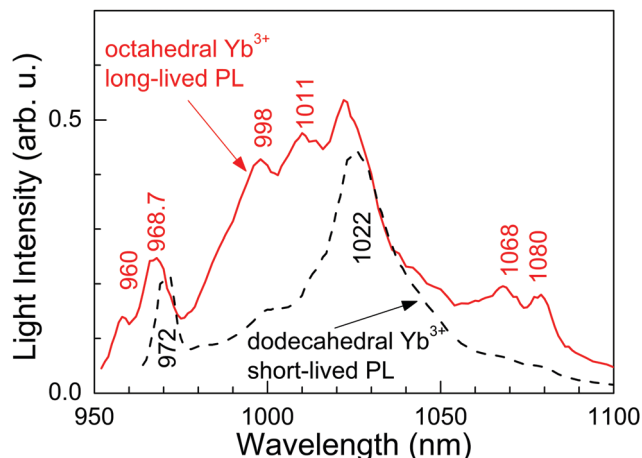

Fig. 5 Comparison of the 300 K OA spectra of 0.3 at%Yb:CNGG (red continuous line) and 11.6 at%Yb:CNGG (black dashed line) crystals. The spectral intensity of the latter crystal is divided by a factor of 170 to equal the intensity of the dodecahedral Yb^{3+} bands (920–944 nm) in both crystals.

7886 | *J. Mater. Chem. C*, 2020, **8**, 7882–7889

This journal is © The Royal Society of Chemistry 2020

dodecahedral Yb^{3+} optical center associated with 24c D_2 symmetry in YAG-like garnets, another minority Yb^{3+} center with very different spectroscopic characteristics coexists in the 0.3 at%Yb:CNGG crystal.

Several CF considerations support the above conclusion. On one side, the experimental energies determined for the m_J levels of the so called 16a octahedral Yb^{3+} center are well reproduced by using a CF parameter set describing a centrosymmetric center, see Table 1. On the other side, the absolute CF splittings of 1069 cm^{-1} and 838 cm^{-1} for ground $^2F_{7/2}$ and excited $^2F_{5/2}$ Yb^{3+} multiplets and their corresponding barycenters, lying at 442 cm^{-1} and 10 632 cm^{-1} energies, respectively, are consistent with those found in other 6-fold oxygen coordinated Yb ionic oxides: in Yb-doped sexquioxides the $^2F_{7/2}$ splitting ranges from 1193 cm^{-1} in Lu_2O_3,[33] to 1076 cm^{-1} in Sc_2O_3.[34] $\Delta E(^2F_{7/2})$ = 1023 cm^{-1} is found for $Ca_4YO(BO_3)_3$ (with 6O-Yb-2B coordination),[35] 964 cm^{-1} in Y_2SiO_5,[34] and 900 cm^{-1} in $Ba_3Lu(BO_3)_3$.[34] Smaller $\Delta E(^2F_{7/2})$ values in 6-fold oxygen coordinated Yb compounds are also found, for instance 788 cm^{-1} in $LiNbO_3$,[36] or even below 600 cm^{-1} in Yb metalorganic complexes,[37] indicating a reduction of the CF strength on Yb^{3+}. In the latter case, a reduction of the effective Yb charge due to covalent bonds of oxygen to the neighboring organic ligands may contribute to the observed CF reduction, while in ionic crystals such CF strength reductions are partially ascribed to larger Yb^{3+} bond distances.

Even when the same Yb^{3+} coordination occurs in a given material the site symmetry influences the $^{2S+1}L_J$ multiplet splitting. Sesquioxides sharing 6-fold oxygen coordinated Yb^{3+} with and without a center of symmetry are a case similar to the present 0.3 at%Yb:CNGG that can guide us for the spectroscopic assignments. While efforts have been made in the assignment of usually experimentally incomplete Yb^{3+} energy level sets both for C_2 and C_{3i} Yb centers of cubic sesquioxides,[38,39] mainly through the application of the barycenter plot law,[34] only CF analyses of 24c dodecahedral Yb^{3+} energy levels have been attempted for garnet hosts.[40,41] These previously known data for cubic sesquioxides indicate that CF splittings of $^2F_{7/2}$ and $^2F_{5/2}$ are always wider and their corresponding barycenters are located at higher energies for centrosymmetric C_{3i} Yb^{3+} centers than for the C_2 ones, see Table 2 in ref. 38 and the ESI† (Table S1). The above indicated splittings for the C_{3i} 16a Yb^{3+} center in the 0.3 at%Yb:CNGG crystal are considerably larger than those of Yb^{3+} in the noncentrosymmetric D_2 24c site in other garnet hosts, for instance, 766 cm^{-1} and 352 cm^{-1} for $^2F_{7/2}$ and $^2F_{5/2}$, respectively, in YbAG, or 624 cm^{-1} and 434 cm^{-1} for YbGG, see Table S2 (ESI†). It could be assumed that larger CF splitting amplitudes for the centrosymmetric C_{3i} 16a Yb^{3+} center are associated with the cooperative effect of considerably smaller bond distances for 16a Yb^{3+} than for Yb^{3+} in the dodecahedral environment as well as with an increase of the symmetry in the 16a center with regard to the 24c one.

The solubility limit for Yb^{3+} incorporation at 16a positions in the CNGG crystal is rather low, obviously below 0.3 at% of the dodecahedral site. From the facts that the background optical absorption at λ = 960.3 nm of dodecahedral Yb^{3+} centers in the 0.3 at%Yb:CNGG crystal is about 50% of the total, see Fig. 5,

and that the total Yb content was estimated from OA comparison as 0.08 at% of the dodecahedral site, the Yb density in the octahedral 16a garnet site can be roughly estimated to be $\approx 5 \times 10^{18}$ cm^{-3}. Such a low limit is in fact expected due to the large Yb^{3+} ionic radii (0.868 Å for VI coordination) compared to those of Nb^{5+} and Ga^{3+} (0.64 Å and 0.62 Å, respectively, also for VI coordination). Due to the low solubility limit for Yb incorporation in the octahedral garnet site, direct evidence of corresponding MD transitions in the OA spectrum will diminish with the increase of Yb content in the crystal, and in fact the same OA bands from 16a Yb^{3+} can be also perceived with very low intensity in the 77 K OA spectrum of the 2 at%Yb:CNGG crystal reported by Voronko et al.,[25] while they are no longer observed in the OA spectrum of the 8 at%Yb:CNGG crystal, see Fig. 2b, since for these latter crystals ED transitions of Yb^{3+} in the dodecahedral garnet site have intensities several orders of magnitude stronger than those of the MD of Yb^{3+} in the octahedral garnet site.

Given that forced ED intraconfigurational f–f Ln^{3+} transitions from the centrosymmetric sites are strictly forbidden, the $^2F_{5/2} \rightarrow ^2F_{7/2}$ emission from 16a Yb^{3+} has a predominant MD character. Consequently, Yb:CNGG is able to provide simultaneously well-differentiated sets of Yb^{3+} $^2F_{7/2} \leftrightarrow ^2F_{5/2}$ ED and MD transitions, arising from 24c and 16a garnet sites, respectively.

The evaluation of the MD contribution of the 16a Yb^{3+} $^2F_{5/2}(0') \rightarrow ^2F_{7/2}(1, 2, 3)$ (λ_{EMI} = 996.7, 1008.7 and 1080.6 nm) transitions can be performed by comparing the total decay rate derived from the measured lifetime value, Γ_{total} = $1/\tau$, with the MD spontaneous emission rate, $A_{MD} = A'_{MD} \times n_r{}^3$, where the vacuum value A'_{MD} is predicted in ref. 12 and n_r = 1.96 is the measured refractive index for CNGG at $\lambda \approx 1000$ nm.[14] The MD branching ratio, defined as $\beta_{MD} = A_{MD}/\Gamma_{total}$, results in $\beta_{MD} \approx$ 50% for 16a Yb^{3+} in CNGG if the room temperature center lifetime is taken as $\tau \approx 4$ ms, see Fig. 4b. This value is similar to previous β_{MD} values indicated for the $^2F_{5/2}(0') \rightarrow ^2F_{7/2}(0)$ Yb^{3+} emission in crystals hosting Yb^{3+} in lattice sites with a center of symmetry, such as SrF_2, Rb_2NaYF_6 or $ScBO_3$.[12] Such crystals are difficult to grow and are not easily available with specific Yb doping, while unfortunately the MD branching ratio of Yb^{3+} in standard YAG is only 10.8%.[12] Therefore, even though the 16a Yb^{3+} center is present in the CNGG garnet with a low density, the strong MD character of its transitions makes them observable, which highlights the interest of the 0.3 at%Yb:CNGG crystal to be used for probing local magnetic fields in plasmonic resonances and metamaterials.

5. Conclusions

A new centrosymmetric octahedral Yb^{3+} center has been identified in the disordered CaNbGa garnet crystal with spectroscopic properties clearly different, both at 6 K and 300 K, from the usual dodecahedral Yb^{3+} center found in this and similar garnets. This new center, which shows favorable properties to be used as a probe for the intensity of magnetic fields radiated by plasmonic structures, operates around λ = 1 μm which is a

good compromise for lithographic fabrication and optical detection techniques. It is characterized by $^2F_{7/2}(0\text{–}3) = 0$, 290, 410, 1069 cm^{-1} and $^2F_{5/2}(0'\text{–}2') = 10\,323$, $10\,413$, $11\,161$ cm^{-1} Yb^{3+} m$_J$ energy levels, which are consistent with the large CF splittings and barycenter energies expected for centrosymmetric Yb^{3+} centers in ionic compounds, their individual positions being well reproduced by a CF simulation assuming a lower, but still with inversion center, D_{4h} symmetry.

The probe center can be operated at room temperature by excitation at $\lambda = 960.3$ nm and with best sensitivity detection near $\lambda = 1080$ nm, although other additional detection channels are found at $\lambda = 998$, 1011 and 1068 nm. The coexistence of dodecahedral and octahedral Yb^{3+} centers in the same crystal with roughly similar densities allows the detection of reference ED and signal MD PL contributions corresponding to the above centers, respectively. Separation of both contributions has been conveniently made by using time-resolved spectroscopy, since ED Yb^{3+} PL is short-lived ($\tau < 0.8$ ms) and the MD one is long-lived ($\tau \approx 4$ ms). The measured MD branching ratio in the studied garnet, $\beta \approx 50\%$, is equivalent to those previously reported in other centrosymmetric hosts, but the easy growth in air of the present CaNbGa garnet with congruent melting at ≈ 1470 °C will facilitate the fabrication of the required plasmonic or metamaterial structures in comparison for instance with Y$_2$O$_3$ whose crystal availability is very limited due to its high melting point of ≈ 2490 °C.

Conflicts of interest

There are no conflicts to declare.

Acknowledgements

References

1 W. T. Carnall, P. R. Fields and K. Rajnak, *J. Chem. Phys.*, 1968, **49**, 4424.
2 Q. Thommen and P. Mandel, *Opt. Lett.*, 2006, **31**, 1803.
3 N. Noginova, G. Zhu, M. Mavy and M. A. Noginov, *J. Appl. Phys.*, 2008, **103**, 07E901.
4 N. Noginova, Y. Barnakov, H. Li and M. A. Noginov, *Opt. Express*, 2009, **17**, 10767.
5 N. Yang, Y. Tang and A. E. Cohen, *Nano Today*, 2009, **4**, 269.
6 X. Ni, G. V. Naik, A. V. Kildishev, Y. Barnakov, A. Boltasseva and V. M. Shalaev, *Appl. Phys. B: Photophys. Laser Chem.*, 2011, **103**, 553.
7 T. H. Taminiau, S. Karaveli, N. F. van Hulst and R. Zia, *Nat. Commun.*, 2012, **3**, 979.
8 S. Karaveli and R. Zia, *Opt. Lett.*, 2010, **35**, 3318.
9 S. Karaveli and R. Zia, *Phys. Rev. Lett.*, 2011, **106**, 193004.
10 M. Kasperczyk, S. Person, D. Ananias, L. D. Carlos and L. Novotny, *Phys. Rev. Lett.*, 2015, **114**, 163903.
11 C. M. Dodson, J. A. Kurvits, D. Li, M. Jiang and R. Zia, *Opt. Mater. Express*, 2014, **4**, 2441.
12 C. M. Dodson and R. Zia, *Phys. Rev. B: Condens. Matter Mater. Phys.*, 2012, **86**, 125102.
13 L. DeLoach, S. Payne, L. Chase, L. Smith and W. Kway, *IEEE J. Quantum Electron.*, 1993, **29**, 1179.
14 E. Castellano-Hernández, M. D. Serrano, R. J. Jiménez-Riobóo, C. Cascales, C. Zaldo, A. Jezowski and P. A. Loiko, *Cryst. Growth Des.*, 2016, **16**, 1480.
15 S. Geller, *Z. Kristallogr.*, 1967, **125**, S1 (and refs. therein).
16 L. Suchow, M. Kokta and V. J. Flynn, *J. Solid State Chem.*, 1970, **2**, 137.
17 L. Suchow and R. Mondegarian, *J. Solid State Chem.*, 1973, **6**, 553.
18 B. V. Mill', *Sov. Phys. Crystallogr.*, 1975, **19**, 653.
19 M. Asano and J. A. Koningstein, *Chem. Phys.*, 1979, **42**, 369.
20 D. Lévy and J. Barbier, *Acta Crystallogr., Sect. C: Cryst. Struct. Commun.*, 1999, **55**, 1611.
21 M. O. Ramírez, L. E. Bausá, E. Cavalli and E. Bovero, *J. Appl. Phys.*, 2006, **99**, 013507.
22 H. G. Liu, W. C. Zheng and W. L. Feng, *Philos. Mag.*, 2008, **88**, 3075.
23 A. Kaminska, M. G. Brik, G. Boulon, M. Karbowiak and A. Suchocki, *J. Phys.: Condens. Matter*, 2010, **22**, 255501.
24 M. D. Serrano, J. O. Álvarez, C. Zaldo, J. Sanz, I. Sobrados, J. A. Alonso, C. Cascales, M. T. Fernández-Díaz and A. Jezowski, *J. Mater. Chem. C*, 2017, **5**, 11481.
25 Y. K. Voronko, A. V. Popov, A. A. Sobol and S. N. Ushakov, *Inorg. Mater.*, 2006, **42**, 1133.
26 V. E. Shukshin, *Phys. Wave Phenom.*, 2009, **17**, 165.
27 V. Lupei, A. Lupei, C. Gheorghe, L. Gheorghe, A. Achim and A. Ikesue, *J. Appl. Phys.*, 2012, **112**, 063110.
28 K. Shimamura, M. Timoshechkin, T. Sasaki, K. Hoshikawa and T. Fukuda, *J. Cryst. Growth*, 1993, **128**, 1021.
29 P. Porcher, M. C. dos Santos and O. Malta, *Phys. Chem. Chem. Phys.*, 1999, **1**, 397.
30 D. S. Sumida and T. Y. Fan, *Opt. Lett.*, 1994, **19**, 1343.
31 E. V. Zharikov, C. Zaldo and F. Díaz, *MRS Bull.*, 2009, **34**, 271 (and refs. therein).
32 J. Liu, X. Mateos, H. Zhang, J. Wang, M. Jiang, U. Griebner and V. Petrov, *Opt. Lett.*, 2005, **30**, 3162.
33 D. C. Brown, Z. Fleischman, L. D. Merkle, L. D. Sanjeewa, C. D. McMillen and J. W. Kolis, *Appl. Phys. B: Photophys. Laser Chem.*, 2020, **126**, 62.
34 P. Haumesser, R. Gaumé, B. Viana, E. Antic-Fidancev and D. Vivien, *J. Phys.: Condens. Matter*, 2001, **13**, 5427.
35 A. Lupei, G. Aka, E. Antic-Fidancev, B. Viana, D. Vivien and P. Aschehoug, *J. Phys.: Condens. Matter*, 2002, **14**, 1107.
36 E. Montoya, J. A. Sanz-García, J. Capmany, L. E. Bausá, A. Diening, T. Kellner and G. Huber, *J. Appl. Phys.*, 2000, **87**, 4056.

37 J. Wang, J. J. Zakrzewski, M. Heczko, M. Zychowicz, K. Nakagawa, K. Nakabayashi, B. Sieklucka, S. Chorazy and S. Ohkoshi, *J. Am. Chem. Soc.*, 2020, **142**, 3970 (and ref. 78 and 79 therein).

38 Y. Guyot, M. Guzik, G. Alombert-Goget, J. Pejchal, A. Yoshikawa, A. Ito, T. Goto and G. Boulon, *J. Lumin.*, 2016, **170**, 513.

39 E. Antic-Fidancev, J. Holsa and M. Lastusaari, *J. Phys.: Condens. Matter*, 2003, **15**, 863.

40 L. Hong-Gang, Z. Wen-Chen and F. Wen-Lin, *J. Lumin.*, 2010, **130**, 103.

41 L. Hong-Gang, G. Paweł and R. Czesław, *J. Lumin.*, 2011, **131**, 2690.

This journal is © The Royal Society of Chemistry 2020

J. Mater. Chem. C, 2020, **8**, 7882–7889 | **7889**